Generic Liver Modelling with Application to Mini-invasive Surgery Guidance

Mathieu Labrunie[1,2], Daniel Pizarro[3,1], Christophe Tilmant[1], and Adrien Bartoli[1,2,4]

[1] EnCoV, Institut Pascal, Université Clermont Auvergne, Clermont-Ferrand, France
mathieu.labrunie@etu.uca.fr
[2] SurgAR, 22 Allée Alan Turing, Clermont-Ferrand, France
[3] Department of Electronics, Universidad de Alcalà, Alcalà de Henares, Spain
[4] DIA2M, DRCI, CHU de Clermont-Ferrand, Clermont-Ferrand, France

Abstract. We propose to guide anatomical or 'patient-generic' (PG) liver modelling by means of 14 anatomical surface point correspondences. We have tested a statistical model built from 71 patient meshes and a generic kernel-based model built from the mean mesh. The latter obtains lower global and local surface reconstruction errors, below 6 mm, while internal structure errors are 11 mm on average. For Mini-Invasive Liver Surgery (MILS) guidance through Augmented Reality (AR), the PG model is registered to an intraoperative 2D image through an adaptation of a patient-specific (PS) 3D/2D registration neural network framework. While this application is slightly less accurate regarding tumour Target Registration Error (TRE) than existing PS methods in in-vivo surgery data, it requires a single training for all patients. It thus eases clinical application and paves the way to anatomical AR through generic anatomical features from the PG model only.

Keywords: Generic Liver Model · MIS · Augmented Reality.

1 Introduction

Liver resections may be non-anatomical or anatomical, respectively removing the tumours with a margin or their enclosing Couinaud segments [7], defined from the main hepatic blood vessels. MILS has tremendous advantages, including reduced trauma and hospital stay. However, it is technically complex because the primary source of intraoperative perception is the surgical camera, which only shows the liver surface and not the inner structures. Intraoperative ultrasound mitigates the issue but is often artefacted and has a long learning curve. In contrast, the preoperative CT or MRI shows the inner structures well. They are valuable yet under-exploited in surgery because bringing them to a consistent AR overlay within the surgical images is highly challenging. This is the 3D-2D registration problem, where one virtually moves and deforms a virtual preoperative 3D liver model constructed from CT or MRI to an intraoperative 2D surgical image. Registration can hardly be done manually during surgery; it is thus highly desirable to use computer vision [20].

The 3D/2D registration methods in MILS use 3D/2D anatomical landmarks [2], namely the anterior ridge [18] as refined in [10] and the liver silhouette [1]. The classical approach uses numerical optimisation. It estimates the pose manually [26] or automatically [9,10] and optionally estimates a deformation field [1,21,10]. The neural approach is more recent [2]. Unlike the graph-based networks for registration with 2D slices [15], the Liver Mesh Recovery (LMR) network [11] is an encoder-regressor [8] which estimates pose and deformation simultaneously from optical 2D projections. It inputs distance maps representing the 2D landmarks and silhouette, which can be automatically provided by an encoder-decoder network [13]. The iterative regressor uses the encoding in addition to an initial pose and deformation for which it outputs updates. It eventually recovers the deformed patient 3D model in camera space. LMR is trained with data simulated from the patient's 3D model [11]. This is a strong limitation: PS LMR performs preoperative simulations and trains the network specifically. This requires expertise, about a day of computation and computational resources for each new patient, hindering usage in clinical practice. In addition, these methods are mainly designed for non-anatomical AR, e.g. segments are not easily visible, and only works if the preoperative images of the patient are available.

Instead, we propose to employ a generic liver shape model. This modelling is highly challenging because of its substantial morphological and localised variations [16,23]. It has been attempted with two approaches. The statistical one uses Statistical Shape Modelling (SSM) with a Point Distribution Model (PDM) [6]. Its construction requires shapes in one-to-one correspondences, obtained using the Coherent Point Drift in [17], a non-rigid point set registration method. The learning-based approach uses the Neural Diffeomorphic Flow (NDF) model [24]. Both try to match liver shapes without any prior knowledge of its anatomy. Though effective in fitting the shapes globally, corresponding parts with high

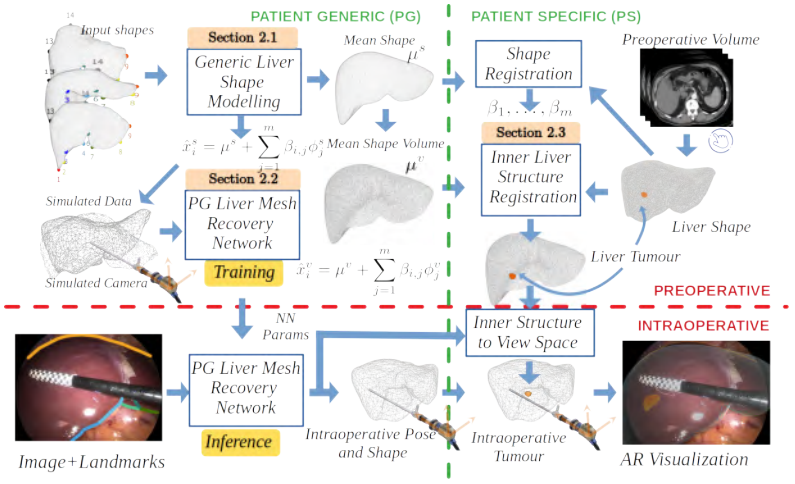

Fig. 1: Proposed PG 3D-2D registration framework in MILS.

morphological differences are likely to mismatch. In order to tackle this issue, we propose to guide the matching through 14 anatomical surface feature point correspondences. This results in much lower surface matching errors. From 71 aligned and matched shapes, we extract a mean shape and use it to model shape by means of a generic kernel or SSM. Both obtain internal vessel point reconstruction errors of the order of 1 cm. The former is selected as it obtains lower surface reconstruction errors. This PG model is applied to the LMR framework instead of the PS preoperative one and enables the first PG neural registration framework for MILS. However, the PS model can be registered to PG one preoperatively. Hence, the same neural model can be used for all patients, without requiring additional training, hence facilitating usage in clinical practice. This also opens the way to a novel type of AR that we call anatomical AR, which consists in overlaying generic anatomical features from the PG liver model only on the surgical images. Anatomical AR does not require preoperative patient data and may reduce navigation time and contribute to surgeon training to MILS.

2 Materials and Methods

Figure 1 shows the proposed general pipeline for 3D-2D registration. The preoperative steps are split into two categories: the PG steps include generic shape modelling and 3D-2D registration network training; the PS steps include inner liver structure registration. These steps are explained in the following sections.

2.1 Generic Liver Shape Modelling

We describe PG liver shape modelling[5]. Our first contribution is the preparation of a dataset of $K = 71$ registered 3D liver mesh models with $n = 4978$ vertices in one-to-one correspondence. We first reconstruct 3D meshes, define manual correspondences, register them densely, and find global correspondences. Our second contribution is two shape models constructed from the prepared data.

We use the first K preoperative CT scans of the v2 AMOS training database, which includes automatic liver segmentation results. We preprocess the data in three steps. First, we manually correct the automatic segmentations, using 3D Slicer. Second, we perform triangular surface mesh reconstruction using marching cubes [12]. Third, we perform Laplacian mesh smoothing from VTK, resampling to 5000 vertices with Approximated Centroidal Voronoï Diagrams [25] using pyacvd, and cleaning [4] from PyMeshFix in order to make it manifold.

Netter's classification [16] shows that the liver has substantial shape variability. The reconstructed liver shapes thus exhibit important local variations, e.g. in the left lobe (figure 2). Non-rigid registration with local correspondence priors is therefore required, which we manually select as sparse point correspondences. Specifically, we propose the 14 anatomical feature points shown in figure 2.

We register surface meshes from a reference one in a pair-wise manner. We select among the K ones, the one which exhibits the most neutral shape. This

[5] Generic modelling data are available in https://encov.ip.uca.fr/ab/code_and_datasets/

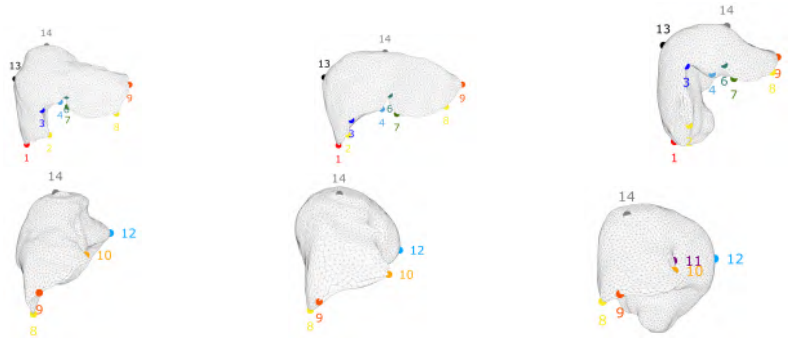

Fig. 2: Liver shape examples, with frontal (top) and left (bottom) views. The proposed correspondences are shown with colour and number coding, 1) extreme lower right, 2) lower anterior right, 3) gallbladder anterior right, 4) anterior right ridge start, 5) rex recessus start, 6) left rex recessus start (usually same as 5), 7) start of the anterior left ridge, 8) extreme anterior lower left, 9) extreme anterior upper left, 10) extreme posterior upper left, 11) vena cava centre, 12) extreme posterior right, 13) extreme upper right, and 14) extreme upper.

model (n°2) has $n = 4978$ vertices. Each other model is successively taken as the registration target, resulting in $K - 1$ deformations of the reference model. We first min-max normalise both the reference and target model coordinates to $[0, 1]^3$. We then proceed in three steps. First, we initialise the deformations with the interpolation of a polyharmonic Radial Basis Functions (RBF) [5] of degree 2 and radius 0.5, from pygem. The RBF control points are deformed from the reference feature points to the target ones. Second, we refine the deformations using Non-Rigid Iterative Closest Point (NR-ICP) [3] of pytorch-nicp. We customise the cost function to use four terms: vertex-to-surface distances, feature point distances and Laplacian smoothing, with respective constant weights of 1, 5, and 100, and stiffness with decreasing weight from 50 to 0.2. We use 50 and 150 iterations respectively in the inner and outer loops. Closest points are known to be asymmetrical between the two sets, we mitigate this issue in performing two runs of NR-ICP. The first takes the reference model as the moving shape. In the second, the registered reference model is taken as the target of the NR-ICP, while the initial one is the moving shape. Third, we eventually compute the correspondences of the n vertices of the reference model using the closest surface points from the final registered shapes.

We construct two models for the liver shape. The first one learns the liver shape from the data using SSM with a PDM. We first run Generalised Procrustes Analysis (GPA) to rigidly align the K shapes and compute the average shape $\mu^{s\top} = [\mu_1^{s\top}, \cdots, \mu_n^{s\top}] \in \mathbb{R}^{3n}$. The two constructed models are linear combinations of m shape components $\phi_j^s = [\phi_{j,1}^s, \cdots, \phi_{j,n}^s]^\top$ for $j = 1, \ldots, m$, so that a shape $\hat{x}_i^s$ can be generated from configuration weights $\beta_i = [\beta_{i,1}, \cdots, \beta_{i,m}]^\top$ as $\hat{x}_i^s = \mu^s + \sum_{j=1}^m \beta_{i,j}\phi_j^s$. The first model then uses Principal Component Anal-

ysis on the K shape data to perform reduced order modelling and using the 'subspace loadings' as shape components. SSM makes the assumption that the shape data are representative of the population of human livers. The second model we construct is more generic, using Gaussian Process Morphable Model (GPMM) [14] with locally-scaled or multi-scale Gaussian kernels, from Statismo. Concretely, this boils down to using combinations of Gaussian processes as shape components, from the mean (template) shape μ^s.

2.2 Patient-generic Liver Mesh Recovery Network

We use the LMR network [11] for performing 3D/2D registration. However, we replace the original PS deformation parameters by the PG shape parameters of the selected model. The training, validation and test set simulations described in [11] are performed accordingly, from 120000 initial simulations. All rotation angle (°) and translation (mm) ranges are respectively set to [−70,70] and [−50, 50] for pose simulations, while keeping the default typical pose. Instead of the preoperative liver mesh used in PS-LMR, the initial one in the proposed PG-LMR uses the mean PG shape μ^s. At inference, distance maps from the annotated landmarks and silhouette of the input image are fed to the network which predicts pose and shape parameters and thus the liver mesh in view space.

2.3 Inner Liver Structure Registration

For PG AR guidance, generic anatomical features, such as the Couinaud segments, are directly found in the PG model and do not need an extra registration. For PS AR guidance, the query inner structures of the actual patient, such as tumours, should be registered to the predicted generic shape volume. This could be achieved in two ways: either using intraoperative volumetric registration for each predicted deformed liver; or preoperative registration for the template shape, which then requires one to transfer the inner structures to the predicted shape. We follow the latter, as its computation load is mostly preoperative. We propose to build a volumetric model $\hat{x}_i^v = \mu^v + \sum_{j=1}^{m} \beta_{i,j} \phi_j^v$, including the shape model such that $\mu^{v\top} = [\mu^{s\top}, \mu^{t\top}]$ where $\mu^{t\top} \in \mathbb{R}^{3p}$ with p the number of inner vertices, and $\phi^v = [\phi^s, \phi^t]$. Importantly, the scores β are common to the volumetric and shape models. First, we compute the volumetric template mesh μ^v using constrained Delaunay tetrahedrisation [22] (DT) from TetGen, where $p = 1106$. We use it for the volumetric GPMM model. Alternatively, we can use a coarser result using classical DT, in which case $p = 0$. We employ it for the 'volumetric' SSM, as our input registered shape samples are only surfacic. In order to find the $\hat{\beta}$ scores associated to the aligned preoperative surface vertices, we then solve the Ordinary Least-Squares problem applied on the linear shape model. We input them to the volumetric model for predicting the volumetric deformed vertices. Then, we compute the barycentric coordinates and associated tetraedra of the patient inner structure vertices with respect to the volumetric template. At inference, the inner structure vertices can be interpolated from the liver vertices predicted by the LMR network, using the volumetric model.

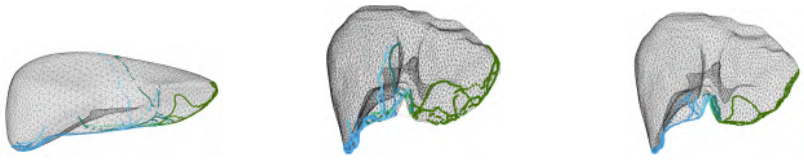

(a) NDF (b) 2 runs of NR-ICP without the feature point term (c) Proposed registration method

Fig. 3: Annotated landmark correspondences on the template after surface registration of RT-GT meshes, using methods a) to c). One colour for each landmark.

Table 1: Average and standard deviation ($\pm$) of the reconstruction errors (mm) of global vertices, feature points and landmarks for both datasets and models. The last column compares the reconstructed landmarks with the annotated ones.

Dataset	AMOS after 2.1		RT-GT			
Object	Global	Features	Global	Features	Landmarks	
Criterion	MAE	MAE	MAE	MAE	MAE	MMD
SSM	2.5 ± 0.3	$\mathbf{3.9 \pm 0.7}$	6.3 ± 0.9	9.0 ± 0.9	7.5 ± 0.9	9.8 ± 2.1
GPMM-L	2.6 ± 0.5	5.6 ± 1.4	3.8 ± 0.3	7.5 ± 0.9	4.1 ± 0.8	7.2 ± 1.3
GPMM-M	$\mathbf{2.0 \pm 0.3}$	4.3 ± 1.0	$\mathbf{3.0 \pm 0.2}$	$\mathbf{5.7 \pm 0.7}$	$\mathbf{3.1 \pm 0.8}$	$\mathbf{6.5 \pm 1.3}$

3 Experimental Results

The main evaluation dataset, referred to as RT-GT, consists of 4 annotated livers where 3D tumour Ground Truth (GT) is retrieved in real annotated laparoscopic images from ultrasound images and appropriate calibrations [19].

We first evaluate the surface registration method. The Mean Mean of closest Distances (MMD) between the registered and annotated landmarks on RT-GT is 4.8 ± 1.0mm. The largest discrepancies are in the landmark endpoints, whose annotation may be subjective. We also compare results between a) NDF [24] which does not use prior knowledge of the anatomy, b) our method without corresponding feature points, i.e. without RBF and the feature point term in the two runs of NR-ICP, and c) our method. NDF is trained using the publicly available code and data. For each RT-GT mesh, we determine the correspondences of the annotated landmarks on the template, i.e the closest registered surface points. The template coordinates are min-max normalised. We evaluate the average MMD between all the pair combinations of the each landmark in the normalised space. The errors are respectively 0.145, 0.132 and 0.033 for a), b) and our method c), showing an improvement factor of 4.4 and 4.0. The same landmarks from different RT-GT patients may have distant shifts on the template for the methods without prior knowledge of the anatomy, see figure 3.

We then evaluate the generic shape models. The liver has an overall length of about 200 mm. We define a first GPMM with a unique Gaussian kernel of standard deviation 20 mm (GPMM-L), to cope with large local variations. We define a second GPMM combining multiple Gaussian kernels of standard deviations 20, 40, 80 and 160 mm (GPMM-M), to deal with several spatial ranges

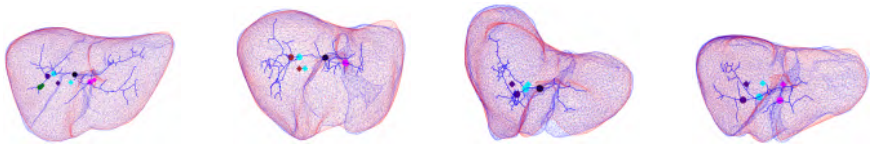

Fig. 4: Inner portal vein bifurcation point registration results (diamonds) and targets (disks) on RT-GT. One colour for each bifurcation. Registered and target livers are respectively in red and blue. The portal vein centreline is also in blue.

Table 2: Average inner portal vein bifurcation registration MAE errors (mm) and standard deviation ($\pm$) for the RT-GT dataset for the different PG models.

Patient	1	2	3	4	Average
SSM	25.3 ± 6.8	20.5 ± 11.5	$\mathbf{9.3 \pm 1.2}$	21.0 ± 1.5	19.0
GPMM-L	20.4 ± 6.0	22.2 ± 10.7	13.0 ± 2.7	$\mathbf{18.9 \pm 3.0}$	18.6
GPMM-M	$\mathbf{14.7 \pm 9.4}$	$\mathbf{12.3 \pm 6.6}$	11.9 ± 4.2	22.3 ± 1.4	**15.3**

of morphological variations. We keep 200 components in both GPMM and 25 in SSM. This allows us to obtain equivalent global vertex reconstruction errors of about 2 mm on AMOS, as shown in table 1. Reconstruction errors are obtained using Mean Absolute distance Error (MAE). On RT-GT, the errors fall between 3 and 4 mm for GPMM models and reach 6.3 mm for SSM. SSM thus does not generalise as well as GPMM, indicating that the training liver shapes may under represent the population. Table 1 also indicates that the 14 correspondences have a higher MAE than both the general vertices and the landmarks, reaching 5.7 mm at minimum for the GPMM-M. This may owe to the uneven sampling density of the feature points around the liver, causing some local parts such as the posterior ones to be less well constrained and reconstructed. The last column of table 1 also indicates the registration errors after model reconstruction. It only reaches 6.5 mm for GPMM-M and almost 10 mm for SSM. In summary, GPMM-M obtains the best surface reconstruction and registration results.

We also compute internal reconstruction and registration errors, using corresponding bifurcation points of the main portal vein branches. AMOS only contains 15 scans where vessels are contrast-enhanced. We partially segment their portal vein and we extract their centreline, using VMTK. Between 2 and 5 corresponding bifurcation points are manually selected, depending on the amount of segmentation. We use the transformation estimates from GPA on the corresponding points in order to obtain the mean internal points in template coordinates. We then compute the barycentric coordinates with respect to the PG volumetric model. This allows us to compute the reconstruction MAE of these internal points on AMOS, respectively $11.3 \pm 4.3, 10.2 \pm 3.9$ and 10.9 ± 4.2 mm for SSM, GPMM-L and GPMM-M models. They are all about 11 mm and higher than surface reconstruction errors, with a higher average standard deviation. Internal inter-subject anatomical differences are not explicitly registered and could thus be partially unrelated to the surface ones. Inner registration (section 2.3) errors of the template vessel bifurcation points are then computed on RT-GT. Table 2

Table 3: Average MAE (mm) and reprojection errors (% of image diagonal) and their standard deviations (±) for the simulated test datasets for the PG-LMR.

Dataset	SSM		GPMM-L		GPMM-M	
Criteria	Reproj.	MAE	Reproj.	MAE	Reproj.	MAE
PG-LMR	3.8 ± 3.1	19.3 ± 10.1	8.0 ± 5.0	30.9 ± 9.9	3.9 ± 2.9	16.8 ± 8.9

Table 4: Average and standard deviation (±) of the TRE for SOTA and proposed PG-LMR for RT-GT, from automatic (A) or manual (M) annotations input to the LMR. Reprojection errors (% of image diagonal) are also given in blue.

Patient	1		2		3		4	
Ann.	A	M	A	M	A	M	A	M
[1]		8.3		37.3		28.4		15.8
[10]	$29.3^{\pm 10.6}$	$10.3^{\pm 2.8}$	$86.9^{\pm 14.7}$	$63.0^{\pm 11.4}$	$30.0^{\pm 60.1}$	$9.5^{\pm 2.1}$	$19.8^{\pm 1.0}$	$14.7^{\pm 1.2}$
PS-LMR	$17.9^{\pm 3.7}$	$17.4^{\pm 4.2}$	$45.6^{\pm 14.7}$	$53.8^{\pm 8.0}$	$46.9^{\pm 7.1}$	$17.6^{\pm 0.6}$	$22.7^{\pm 9.1}$	$17.0^{\pm 0.8}$
PG-LMR	$35.4^{\pm 13.3}$	$22.8^{\pm 6.1}$	$42.9^{\pm 12.6}$	$60.1^{\pm 22.3}$	$40.2^{\pm 2.8}$	$49.4^{\pm 2.5}$	$23.2^{\pm 4.2}$	$14.6^{\pm 1.8}$
	$2.4^{\pm 0.9}$	$1.5^{\pm 0.5}$	$5.7^{\pm 2.1}$	$3.3^{\pm 0.3}$	$2.4^{\pm 0.3}$	$2.9^{\pm 0.2}$	$5.3^{\pm 1.8}$	$4.3^{\pm 1.1}$

shows that GPMM-M obtains the best average results of 15.3 mm, between 11.9 and 22.3 mm for all patients, shown in figure 4. This is slightly larger than the reconstruction ones obtained for AMOS, probably due to limited representativeness of the 15 samples. SSM obtains the worse average results of 19 mm, which could be due to its coarse DT. GPMM-M is thus selected as the PG model.

We can then evaluate the 3D-2D registration method. LMR was trained for the PG model in 31 epochs. The registration results for all the simulated test datasets (section 2.2) are shown in table 3, namely the reprojection error, which is the mean of the mean closest distances of the projected landmark and silhouette vertices from corresponding targets, and the MAE between the predicted and simulated surface liver vertices. Average errors are higher for the GPMM-L set which, owing to very high synthetic local variations, is more difficult to fit. PG-LMR obtains an MAE between 16.8 and 19.3 mm and reprojection errors around 4% of the image diagonal on both SSM and GPMM-M sets.

On RT-GT, reprojection errors are of the same order: between 1.5 and 4.3% and between 2.4 and 5.7% of the image diagonal are respectively obtained for manual and automatic annotations, see table 4, and look rather low, as illustrated in figure 5. Regarding tumour position evaluation, TRE [19] is computed. We compare the results to state-of-the-art methods [1,10,11] in table 4. TREs for our method are marginally larger than for the PS-LMR, except for Patient 3 where it is 3 cm higher. This discrepancy between TRE and reprojection errors suggests that there are registration ambiguities, i.e. several shapes could correspond to the 2D landmarks. Initialising the shape from the predicted patient scores $\hat{\beta}$ at inference could alleviate this issue. In a broader perspective, the PG-LMR shares the architecture of the PS-LMR and thus has the same advantages of runtime in OR, unlike optimisation-based methods. However, it outperforms in deployability due to the single training for all patients. It also facilitates anatomical AR, illustrated in figure 5, as it only requires generic anatomical data related to the PG model. These assets would also ease surgeon education.

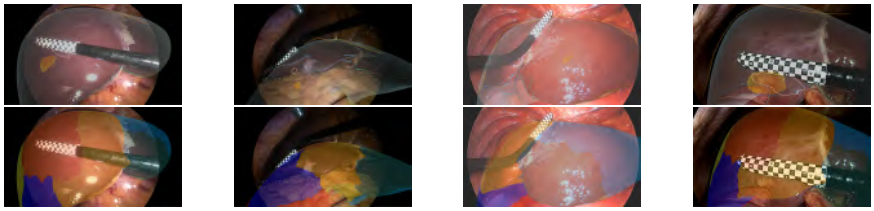

Fig. 5: PS (top) and PG (bottom) AR results from PG-LMR on RT-GT samples, respectively showing the predicted (orange) and GT (pink) tumours and coarse Couinaud segments, manually defined on the PG template.

4 Conclusion

We have proposed 1) a novel generic liver shape registration and modelling methods using prior anatomical knowledge, through surface feature points, highly reducing surface registration and reconstruction errors, 2) the first PG neural 3D-2D registration framework for MILS, making use of 1) and facilitating both PS and PG image augmentation. Unlike previous work, our framework does not require per-patient retraining and is applicable without PS data. In future work, we plan to 1) extend the number and area (e.g. using the hepatic vein) of internal correspondences in order to thoroughly characterise the gap between surface and internal inter-subject anatomical differences and build the generic Couinaud segments accordingly, 2) evaluate feature point annotation inter-operator variability, 3) improve registration accuracy, slightly subpar PS methods, by initialising the registration closer to the patient shape, and 4) evaluate the potential of anatomical augmentation in surgical navigation and surgeon training.

Acknowledgments. M. Labrunie is supported by a CIFRE PhD fellowship (N 2021/0184) from ANRT under partnership between EnCoV and SURGAR.

References

1. Adagolodjo, Y., Trivisonne, R., Haouchine, N., Cotin, S., Courtecuisse, H.: Silhouette-based pose estimation for deformable organs application to surgical augmented reality. In: IROS. pp. 539–544 (2017)
2. Ali, S., Espinel, Y., Jin, Y., Liu, P., Güttner, B., et al.: An objective comparison of methods for augmented reality in laparoscopic liver resection by preoperative-to-intraoperative image fusion. arXiv preprint arXiv:2401.15753 (2024)
3. Amberg, B., Romdhani, S., Vetter, T.: Optimal step nonrigid ICP algorithms for surface registration. In: CVPR. pp. 1–8 (2007)
4. Attene, M.: A lightweight approach to repairing digitized polygon meshes. The visual computer **26**, 1393–1406 (2010)
5. Buhmann, M.D.: Radial basis functions. Acta numerica **9**, 1–38 (2000)
6. Cootes, T.F., Taylor, C.J., Cooper, D.H., Graham, J.: Training models of shape from sets of examples. In: BMVC. pp. 9–18. Springer (1992)
7. Couinaud, C.: Le foie: études anatomiques et chirurgicales. Masson (1957)

8. Kanazawa, A., Black, M.J., Jacobs, D.W., Malik, J.: End-to-end recovery of human shape and pose. In: CVPR. pp. 7122–7131 (2018)
9. Koo, B., Robu, M.R., Allam, M., Pfeiffer, M., Thompson, S., Gurusamy, K., Davidson, B., Speidel, S., Hawkes, D., Stoyanov, D., et al.: Automatic, global registration in laparoscopic liver surgery. IJCARS **17**(1), 167–176 (2022)
10. Labrunie, M., Ribeiro, M., Mourthadhoi, F., Tilmant, C., Le Roy, B., Buc, E., Bartoli, A.: Automatic preoperative 3d model registration in laparoscopic liver resection. IJCARS pp. 1–8 (2022)
11. Labrunie, M., Pizarro, D., Tilmant, C., Bartoli, A.: Automatic 3d/2d deformable registration in minimally invasive liver resection using a mesh recovery network. In: MIDL (2023)
12. Lorensen, W.E., Cline, H.E.: Marching cubes: A high resolution 3d surface construction algorithm. In: SIGGRAPH, pp. 347–353 (1998)
13. Lu, X., Wang, W., Ma, C., Shen, J., Shao, L., Porikli, F.: See more, know more: Unsupervised video object segmentation with co-attention siamese networks. In: CVPR. pp. 3623–3632 (2019)
14. Lüthi, M., Gerig, T., Jud, C., Vetter, T.: Gaussian process morphable models. TPAMI **40**(8), 1860–1873 (2017)
15. Nakao, M., Nakamura, M., Matsuda, T.: Image-to-graph convolutional network for 2d/3d deformable model registration of low-contrast organs. T-MI **41**(12), 3747–3761 (2022)
16. Netter, F.H.: Atlas of human anatomy E-Book. Elsevier health sciences (2014)
17. Pellicer-Valero, O.J., Rupérez, M.J., Martínez-Sanchis, S., Martín-Guerrero, J.D.: Real-time biomechanical modeling of the liver using machine learning models trained on finite element method simulations. Expert Syst Appl **143**, 113083 (2020)
18. Plantefève, R., Haouchine, N., Radoux, J.P., Cotin, S.: Automatic alignment of pre and intraoperative data using anatomical landmarks for augmented laparoscopic liver surgery. In: Biomedical Simulation (2014)
19. Rabbani, N., Calvet, L., Espinel, Y., Le Roy, B., Ribeiro, M., Buc, E., Bartoli, A.: A methodology and clinical dataset with ground-truth to evaluate registration accuracy quantitatively in computer-assisted laparoscopic liver resection. Comput Methods Biomech Biomed Eng Imaging Vis pp. 1–10 (2021)
20. Ramalhinho, J., Yoo, S., Dowrick, T., Koo, B., Somasundaram, M., Gurusamy, K., Hawkes, D.J., Davidson, B., Blandford, A., Clarkson, M.J.: The value of augmented reality in surgery—a usability study on laparoscopic liver surgery. MedIA **90**, 102943 (2023)
21. Robu, M.R., Ramalhinho, J., Thompson, S., Gurusamy, K., Davidson, B., Hawkes, D., Stoyanov, D., Clarkson, M.J.: Global rigid registration of CT to video in laparoscopic liver surgery. IJCARS **13**(6), 947–956 (2018)
22. Shewchuk, J.R.: Constrained delaunay tetrahedralizations and provably good boundary recovery. In: IMR. pp. 193–204. Citeseer (2002)
23. Singh, H.R., Rabi, S.: Study of morphological variations of liver in human. Transl Res Anat **14**, 1–5 (2019)
24. Sun, S., Han, K., Kong, D., Tang, H., Yan, X., Xie, X.: Topology-preserving shape reconstruction and registration via neural diffeomorphic flow. In: CVPR. pp. 20845–20855 (2022)
25. Valette, S., Chassery, J.M.: Approximated centroidal voronoi diagrams for uniform polygonal mesh coarsening. In: CGF. vol. 23, pp. 381–389. WOL (2004)
26. Özgür, E., Koo, B., Le Roy, B., Buc, E., Bartoli, A.: Preoperative liver registration for augmented monocular laparoscopy using backward-forward biomechanical simulation. IJCARS **13**(10), 1629–1640 (2018)